Time-dependent effects using selective-excitation double-Mössbauer techniques with application to α-Fe_2O_3†

Bohdan Balko* and Gilbert R. Hoy
Boston University, Boston, Massachusetts 02215
(Received 2 August 1973)

Selective-excitation double-Mössbauer (SEDM) experiments have been done using powdered scatterers of iron and α-Fe_2O_3. In addition, calculations have been made to predict the SEDM line shape. These calculations included Rayleigh, incoherent electronic, and thickness effects. The scatterer was assumed to have a six-line Mössbauer transmission spectrum. SEDM line shapes are calculated for both static and dynamic ^{57}Fe nuclear environments. Results for static SEDM line shapes involving one transition show that the scattered radiation consists of a single peak located at the excitation energy for scatterer thicknesses $\beta > 20$. This is not true in the dynamic case. SEDM procedures are shown to be superior to ordinary Mössbauer transmission experiments in determining time-dependent effects in certain cases. We have applied these methods to study the Morin transition in α-Fe_2O_3. Our results show that each iron nucleus is in a fluctuating hyperfine field. The values of the relaxation times at 263.5, 261, 259.5, and 258.5 K are $(1.1 \pm 0.2) \times 10^{-7}$, $(2.3 \pm 0.4) \times 10^{-7}$, $(2.9 \pm 0.6) \times 10^{-7}$, and $(4.3 \pm 0.9) \times 10^{-7}$ sec.

I. INTRODUCTION

The selective-excitation double-Mössbauer effect (SEDM) has already been demonstrated by other investigators.[1–3] However, in their work no attempt was made to compare SEDM spectra with detailed calculations. In this paper we do that, and then proceed to develop part of the necessary analysis for applying the technique to the study of time-dependent hyperfine interactions.

The basic SEDM apparatus, shown in Fig. 1, requires two Doppler modulators. The first one drives a single-line Mössbauer source at a constant velocity (CVD), exciting the desired nuclear level in the scatterer, which is made of the material under investigation. The other drive (CAD) moves a single-line absorber, called the analyzer, and is used in the usual transmission geometry to analyze the scattered radiation.

In Mössbauer transmission and single-drive scattering experiments the measured quantity is essentially the absorption cross section. This absorption cross section is affected by time-dependent hyperfine interactions, but sometimes this effect cannot be distinguished from static perturbations such as, internal field inhomogeneities. In addition, these regular Mössbauer results often contain many lines, and are difficult to unravel. In the SEDM case, the measured quantity is the differential scattering cross section which is a function of the incoming and outgoing photons. In particular, the incoming beam energy is set at a known value and the energy distribution of the outgoing radiation is measured. Consequently, information about energy transformations in the scatterer during the lifetime of the nuclear state can be directly observed. For example, if relaxation is occurring in the scatterer, the SEDM spectrum under favorable conditions will show *extra* lines, which would not appear in SEDM spectra for the time-independent case. The exact line shape, which is discussed below, depends on several factors. However, the information content of an SEDM spectrum includes not only direct evidence for relaxation and the value of the relaxation rate, but also the energy levels which are coupled by the relaxation process.

II. EXPERIMENTAL SETUP AND PROCEDURES

The characteristic feature of SEDM experiments is that four recoilless events constitute a measurement, and therefore two Doppler modulators have to be used to test for their occurrence. A block diagram of the SEDM apparatus is shown in Fig. 1. The components comprising the Doppler modulators are of conventional design and utilize the electromechanical driving technique. The two mechanical drives were constructed according to the National Bureau of Standards design[4] and are identical. The CVD drive followed the rectangular signal which was obtained from a bistable multivibrator activated by a photocell pulser as described by Ruegg *et al.*[5] The excitation velocity was set at the required level and the return velocity was set sufficiently beyond the other scatterer resonances so that no other energy levels were excited.

Drive No. 2 was used in the constant-acceleration mode (CAD). A triangular input signal was obtained from a function generator described by Cohen.[6] This signal was used in experiments when the complete hyperfine pattern was required. When doing SEDM experiments the input signal to drive No. 2 was derived from a trapezoidal function

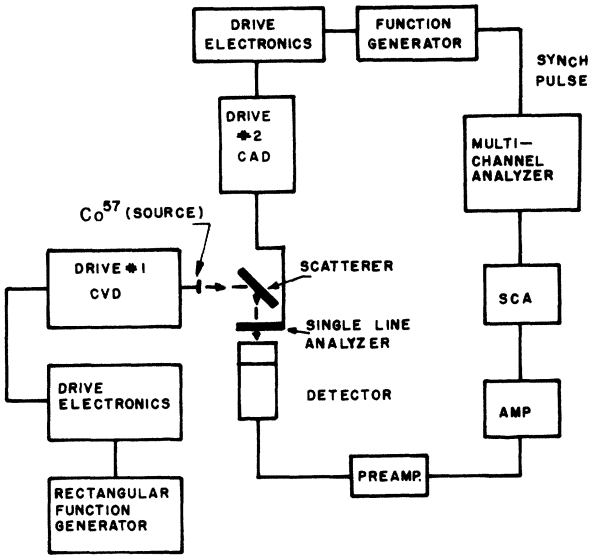

FIG. 1. Schematic block diagram of the SEDM apparatus.

generator.[7] This allowed us to study a selected section of the spectrum in detail at high-energy resolution. The power amplifier and feedback circuits are standard and are described elsewhere.[8]

In the early stages of this research, we used a solid-state detector [Kevex 1000, Si(Li)], but a proportional counter (Reuter-Stokes model RSG-61) filled with $XeCO_2$ at 2 atm was finally chosen and used in most of the experiments. Its energy resolution compares well with that of the Si(Li) detector, and it gives a much higher counting rate.

The source, purchased from New England Nuclear, was made by electroplating 45 mCi of ^{57}Co onto a copper foil 25 μ thick and 12 mm in diameter. The active area is 6 mm in diameter. The scatterers were made from commercially available 90%-enriched and natural α-Fe_2O_3 and Fe-metal powders. The powder was pressed onto a thin lucite disk coated with vacuum grease, and the surface facing the beam was covered with a sheet of "Saran wrap." This combination was pressed into an aluminum frame and held in place by a tightly fitting plug. The frame was supported in the path of the beam by a thin rod attached to a reference stand which allowed the scatterer to be rotated around a vertical axis. The analyzer was a single-line $Na_4Fe(CN)_6 \cdot 10H_2O$ absorber having a thickness parameter $\beta = 14$ ($\beta = n'' \sigma_0 f$, where n'' is the number of ^{57}Fe atoms/cm^2, σ_0 the resonance cross section, and f the recoilless fraction).

To obtain sample temperatures different from room temperature, a Dewar purchased from Andonian Associates Inc. was used. The tail section was modified to allow scattering angles of 90 and 60°. Two Cu-constantan thermocouples in series were used along with a control unit to regulate the temperature. This was done by switching a heater (1.24 W) on and off. The heater was mounted just above the sample. We used dry ice in methanol in the inner container of the Dewar as the coolant. Two Cu-constantan thermocouples, one referenced at the melting point of ice and the other at liquid nitrogen, were used to monitor the temperature of the sample. It was found that temperature regulation to 0.5 °C could be obtained.

It is very important in performing scattering and SEDM experiments to provide proper shielding of the detector from unwanted radiation. Our arrangement with the Dewar in place, is shown in Fig. 2. The analyzer holder rod actually moves through a hole in the lead brick and is located about $\frac{1}{4}$ in above the rod holding the source. All the surfaces facing the beam are either made of brass or covered with $\frac{1}{16}$ in-thick copper plate to absorb the lead x ray.

The experimental procedure for conducting SEDM experiments is as follows.

(i) A normal Mössbauer transmission spectrum using the constant-acceleration mode and a triangle wave form is obtained. This spectrum is needed to perform and interpret SEDM experiments. From this spectrum a correspondence between the output (LVsyn) voltage and line position can be calculated, which is useful in setting up the SEDM runs.

(ii) Drive No. 1 is now used in the CVD mode to

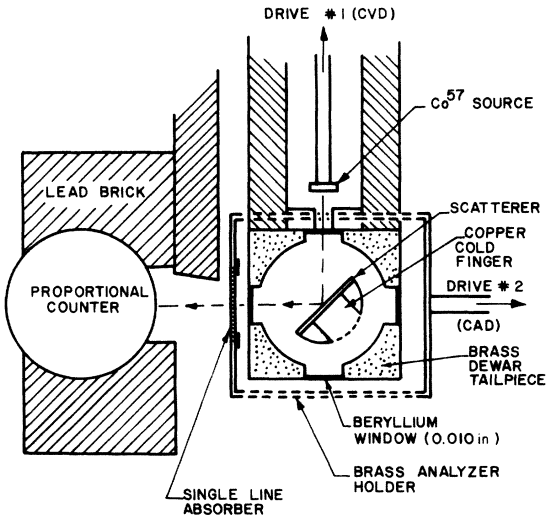

FIG. 2. SEDM shielding arrangement. The sections of the analyzer holder shown in dashed lines are actually $\frac{1}{4}$ in. above (top part) and below (bottom part) the plane defined by the incident and scattered radiation directions.

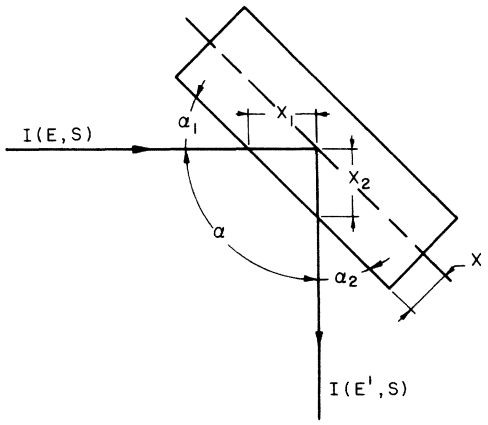

FIG. 3. Scatterer orientation relative to the incident and scattered radiation directions.

obtain a transmission spectrum of the material over a selected region of velocities, i.e., the peak to be excited in the SEDM experiment and possibly another peak for calibration purposes.

(iii) The CVD (Drive No. 1) is now set to excite the line of interest in the scatterer. With the detector in the 90°-scattering geometry and the CAD (Drive No. 2) moving according to a trapezoidal (or triangular) wave form the SEDM experiment begins.

(iv) At selected intervals the CAD- and CVD-drive calibrations should be checked by conducting transmission experiments as in steps (i) and (ii). Our experiments lasted anywhere from four days to two weeks and the calibrations were checked every three or four days.

The SEDM spectra obtained in this way, as well as the transmission and single-drive scattering spectra, were initially analyzed using a computer program developed in our laboratory.[9] This program corrects for the parabolic background and, among other things, computes a least-squares fit to the experimental data, assuming Lorentzian line shapes. The final analysis of the SEDM spectra was done by using the results of Sec. III for the time-independent case, or Sec. IV for the time-dependent case, whichever is appropriate (see below). In analyzing SEDM experiments it is important to know the energy distribution of the source radiation. This distribution, which includes thickness effects in the source, finite source area, collimation, and mechanical distortions, was measured by conducting constant-velocity transmission experiments using Drive No. 1 and a thin absorber. The measured effective linewidth of our ^{57}Co in Cu source was $\Gamma_{\text{eff}} = 2.3\Gamma$, where $\Gamma = 0.097$ mm/sec.

III. SEDM THEORETICAL RESULTS WITHOUT TIME-DEPENDENT EFFECTS

In this section we calculate the energy spectral distribution of radiation that reaches the detector after being scattered by a "split," "thick" scatterer and transmitted through the analyzer. The major effects that need to be considered are Mössbauer processes characterized by the resonant cross section σ_0, Rayleigh events characterized by σ_R, and the electronic extinction coefficient μ_e of the scatterer which characterizes the other processes that attenuate the intensity of the radiation as it traverses the scatterer. We neglect coherent thickness effects[10] and multiple scattering. We only mention coherent thickness effects for completeness. These effects only apply to single crystals at Bragg angles or at most to mosaic specimens. They are very difficult to even observe at all. The neglect of multiple scattering is justified by our results, and in any event contributes, in our case, at most a 1% effect.

Consider the situation as shown in Fig. 3. The intensity distribution of the source radiation, assumed to be Lorentzian, is $I(E, S)$, where S is the Doppler energy set by the CVD. The intensity of the radiation reaching a distance x into the scatterer is,

$$I_x(E, S) = I(E, S) \exp[-\mu_T(E) \csc\alpha_1 x], \tag{1}$$

where α_1 is the angle of the incoming beam relative to the scatterer and $\mu_T(E)$ is the scatterer's total absorption coefficient. The scatterer's total linear absorption coefficient $\mu_T(E)$ can be decomposed into three parts: nuclear resonant $\mu_M(E)$, coherent nonresonant μ_R (including electronic Rayleigh and nuclear Thomson scattering), and the electronic absorption coefficient μ_e which includes all incoherent, essentially energy-independent, scattering processes. Thus,

$$\mu_T(E) = \mu_M(E) + \mu_R + \mu_e . \tag{2}$$

The resonant nuclear absorption can take place at energies corresponding to the allowed nuclear transitions E_{ij}. If the nuclear energy levels are pure-m states,

$$\mu_M(E) = \sum_{i,j} \frac{nf\sigma_0(\frac{1}{2}\Gamma)^2}{(E - E_{ij})^2 + (\frac{1}{2}\Gamma)^2} W_{ij}(\theta_1 \phi_1), \tag{3}$$

where f is the scatterer's recoilless fraction, n is the number of resonant nuclei per unit volume, Γ is the natural linewidth, and σ_0 is the maximum resonant absorption cross section. The scattering angles are defined in Fig. 4(a). The functions $W_{ij}(\theta_1, \phi_1)$ are[11]

$$W_{ij} = |C(I_e m_j | LMI_g m_i)|^2 |\vec{X}_L^M(\theta_1, \phi_1)|^2 . \tag{4}$$

Here the C's are the usual Clebsch-Gordan coef-

ficients and the $\vec{X}_L^{M'}$s are vector spherical harmonics.

We first consider the nuclear resonant contribution. In general this term contributes a part from recoilless absorption and recoilless emission and another part from recoilless absorption and nonrecoilless emission. However, since the scattered radiation is analyzed using the Mössbauer effect in the analyzer, we only need consider the recoilless-recoilless part. The energy distribution per unit length per unit solid angle of the radiation scattered at x by resonant nuclear processes is

$$\frac{d}{dx} I_M(E', S) = \int dE\, I_x(E, S)\, nf \frac{d^2\sigma_M}{dE\, dE'} . \tag{5}$$

Following Heitler,[12] and Boyle and Hall[13] we can write the differential scattering cross section as,

$$\frac{d^2\sigma_M}{dE\, dE'} = \sum_{i,j,i'} \frac{f\sigma_0 W_{ij}(\theta_1\phi_1) W_{ji'}(\theta_2\phi_2)(\frac{1}{2}\Gamma)^2}{(1+a')[(E-E'+\Delta_{ii'})^2+(\frac{1}{2}\gamma)^2][(E'-E_{ij}-\Delta_{ii'})^2+(\frac{1}{2}\Gamma)^2]} , \tag{6}$$

where a' is the internal conversion coefficient, and γ is the linewidth due to the source intensity and hence is very small; we have allowed for absorption between the nuclear levels $E_i^g \rightarrow E_j^e$ to result in the decays $E_j^e \rightarrow E_i^g$ and $E_j^e \rightarrow E_{i'}^g$. [$E_{ij} = E_j^e - E_i^g$ and $\Delta_{ii'} = E_i^e - E_{i'}^g = G$ (see Fig. 4).] In the above sum we must include all transitions consistent with the selection rules.

We assume that the source radiation has a Lorentzian line shape and neglect any anisotropic f dependence. Substituting Eqs. (6) and (1) into Eq. (5) and integrating over E gives,

$$\frac{dI_M}{dx}(E', S) = \sum_{i,j,i'} \frac{I_0 nf^2\sigma_0(\frac{1}{2}\Gamma_b)^2(\frac{1}{2}\Gamma)^2 \exp[-\mu_T(E'-\Delta_{ii'})\csc\alpha_1 x] W_{ij} W_{ji'}}{(1+\alpha')[E'-\Delta_{ii'}-S)^2+(\frac{1}{2}\Gamma_b)^2][(E'-E_{ij}-\Delta_{ii'})^2+(\frac{1}{2}\Gamma)^2]} , \tag{7}$$

where Γ_b is the effective linewidth of the incident beam. Neglecting multiple scattering, the energy distribution of the nuclear resonant scattered radiation that gets to the analyzer is

$$I_M(E', S) = \int_0^T \frac{d}{dx} I_M(E', S) \exp[-\mu_T(E') \csc\alpha_2 x]\, dx ,$$

where T is the thickness of the scatterer. The result is

$$I_M(E', S) = \sum_{i,j,i'} \frac{nf^2\sigma_0 I_0(\frac{1}{2}\Gamma_b)^2(\frac{1}{2}\Gamma)^2 W_{ij} W_{ji'} F}{(1+\alpha')[(E'-\Delta_{ii'}-S)^2+(\frac{1}{2}\Gamma_b)^2][(E'-E_{ij}-\Delta_{ii'})^2+(\frac{1}{2}\Gamma)^2]} , \tag{8}$$

where

$$F = \frac{1-\exp\{-T[\mu_T(E'-\Delta_{ii'})\csc\alpha_1 + \mu_T(E')\csc\alpha_2]\}}{\mu_T(E'-\Delta_{ii'})\csc\alpha_1 + \mu_T(E')\csc\alpha_2} .$$

Equation (8) is essentially the same as found in Debrunner and Morrison[14] but generalized to a "split" scatterer. The angular distribution of the resonantly scattered radiation is represented by $W_{ij}(\theta_1, \phi_1) \times W_{ji'}(\theta_2, \phi_2)$. If the scatterer is a powder, this factor must be averaged subject to the constraint that the scattering angle α is constant. We can denote this result by $W_{ij,ji'}(\alpha)$. These vaules are calculated and tabulated in Appendix A. For calculational purposes it is convenient to use a notation where the transitions are labeled by the lines themselves as shown in Fig. 4. Then Eq. (8) can be written

$$\begin{aligned} I_M(E', S) = nA_M \Bigg(& \sum_{i=1}^{6} \frac{W_{i,i}(\alpha)}{(E'-E_i)^2+(\frac{1}{2}\Gamma)^2} \frac{1-\exp[-T(\csc\alpha_1+\csc\alpha_2)\mu_T(E')]}{[(E'-S)^2+(\frac{1}{2}\Gamma_b)^2](\csc\alpha_1+\csc\alpha_2)\mu_T(E')} \\ & + \sum_{i=2}^{3} \frac{W_{i,i+2}(\alpha)(1-\exp\{-T[\mu_T(E'-G)\csc\alpha_1+\mu_T(E')\csc\alpha_2]\})}{[(E'-E_i-G)^2+(\frac{1}{2}\Gamma)^2][(E'-S-G)^2+(\frac{1}{2}\Gamma_b)^2][\mu_T(E'-G)\csc\alpha_1+\mu_T(E')\csc\alpha_2]} \\ & + \sum_{i=2}^{3} \frac{W_{i+2,i}(\alpha)(1-\exp\{-T[\mu_T(E'+G)\csc\alpha_1+\mu_T(E')\csc\alpha_2]\})}{[(E'-E_{i+2}+G)^2+(\frac{1}{2}\Gamma)^2][(E'-S+G)^2+(\frac{1}{2}\Gamma_b)^2][\mu_T(E'+G)\csc\alpha_1+\mu_T(E')\csc\alpha_2]} \Bigg) , \end{aligned} \tag{8}$$

where G equals the ground-state splitting,

$$\mu_T(E') = \sum_{i=1}^{6} \frac{nf\sigma_0(\frac{1}{2}\Gamma)^2 \bar{W}_i}{[(E'-E_i)^2+(\frac{1}{2}\Gamma)^2]} + \mu_R + \mu_e ,$$

the bar indicates an average over all angles (see Appendix A), and A_M is a constant determined by the particular experiment.

The coherent nonresonant contribution to the scattered intensity is mostly Rayleigh, because at these energies the Rayleigh contribution is $\sim 10^4$

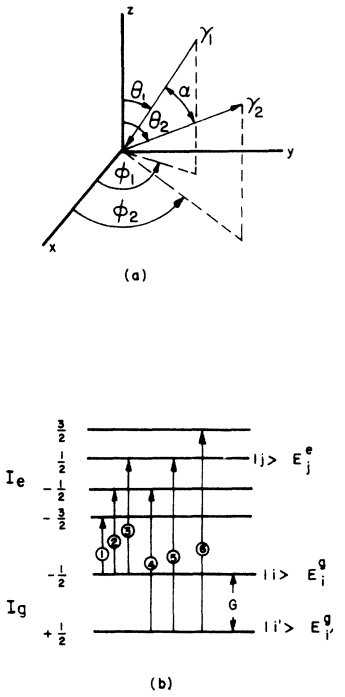

FIG. 4. (a) Definition of the angles used in the scattering calculations. (b) Energy-level diagram for a "split" ^{57}Fe scatterer. The allowed transitions are labeled 1, 2, 3, 4, 5, and 6.

times the Thomson contribution.[15] The energy dependence of the Rayleigh cross section is relatively weak and so,

$$I_R(E',S)=\frac{I_0(\frac{1}{2}\Gamma_b)^2 n' f_R \sigma_R W_R(\alpha)}{(E'-S)^2+(\frac{1}{2}\Gamma_b)^2} \times\left(\frac{1-\exp[-\mu_T(E')(\csc\alpha_1+\csc\alpha_2)T]}{\mu_T(E')(\csc\alpha_1+\csc\alpha_2)}\right), \tag{10}$$

where n' is the number of atoms per volume, f_R is the recoilless fraction for Rayleigh scattering ($f_R=f^2$ for $\alpha=90°$),[16] σ_R is the Rayleigh cross section evaluated at 14 keV (for our purposes), and[15]

$$W_R(\alpha)=\frac{1+\cos^2\alpha}{\sin^3\frac{1}{2}\alpha} .$$

Collecting energy-independent factors,

$$I_R(E',S)=\frac{n' A_R\{1-\exp[-\mu_T(E')(\csc\alpha_1+\csc\alpha_2)T]\}}{[(E'-S)^2+(\frac{1}{2}\Gamma_b)]\,\mu_T(E')(\csc\alpha_1+\csc\alpha_2)} . \tag{11}$$

In general the energy distribution of the scattered radiation contains an interference term from the nuclear resonant and coherent Rayleigh-scattering processes. However at a scattering angle $\alpha=90°$ this interference term is zero.[17] Because of the unavoidable experimental angular spread about 90° we have made estimates of the size of the interference term. For our case, the ratio of the interference term to the terms we included in the calculation is, 7×10^{-6} for excitation on resonance and 3×10^{-3} for excitation 10 natural linewidths off resonance. As will be seen below our experiments do not show interference effects and any line-shape asymmetry is not due to this effect.[18] Under these circumstances the two contributions can be calculated separately and added. The total energy-dependent intensity distribution of the scattered radiation, which is subject to analysis by the analyzer in transmission geometry, is

$$I(E',S)=I_M(E',S)+I_R(E',S), \qquad I(E',S)=\text{Eq. (9)}+\text{Eq. (11)} . \tag{12}$$

Once $I(E',S)$ is determined the effect of the analyzer can be calculated by

$$I(S,S')=\int_0^\infty I(E',S)\,e^{-\mu_a(E',S')T_a}dE' , \tag{13}$$

where S' is the Doppler energy of the "single-line" analyzer and

$$\mu_a=\frac{n_a f_a \sigma_0(\frac{1}{2}\Gamma)^2}{(E'-S'-E_0)^2+(\frac{1}{2}\Gamma)^2} =\frac{\beta_a(\frac{1}{2}\Gamma)^2}{[(E'-S'-E_0)^2+(\frac{1}{2}\Gamma)^2]T_a} .$$

Computer programs have been written to solve all of the above equations.

All our experiments were done using ^{57}Fe, and the calculations were performed assuming that the nuclear levels are pure-m states. As noted above, $\alpha=90°$ and $\alpha_1=\alpha_2=45°$. The E_i's and G can be determined by ordinary transmission experiments. The total linear absorption coefficient, $\mu=\mu_R+\mu_e$, was determined experimentally for both iron and α-Fe_2O_3 samples by measuring the attenuation of the γ-ray beam on passing through various sample thicknesses. The values obtained were $\mu=205$ cm^{-1} for iron and $\mu=54$ cm^{-1} for α-Fe_2O_3. The relative strength of Rayleigh to Mössbauer processes, i.e., A_R/A_M [see Eqs. (9) and (11)] must be determined for each experiment although in ideal cases it can be calculated.[15] This calculated result was checked by performing the experiment shown in Fig. 5(b) and subsequent experiments presented below. In Fig. 5(b) only the peak on the left has a Rayleigh contribution. By comparing the experimental results with calculations from Eq. (13), we found $(A_R/A_M)=4\times10^{-5}$ for the 90%-enriched sample of α-Fe_2O_3. This number was further checked by exciting the same peak at different values off resonance and again comparing them with the results from Eq. (13).

In order to get a feeling for these calculations let us consider a hypothetical scatterer in which the hyperfine field is zero, i.e., the absorption

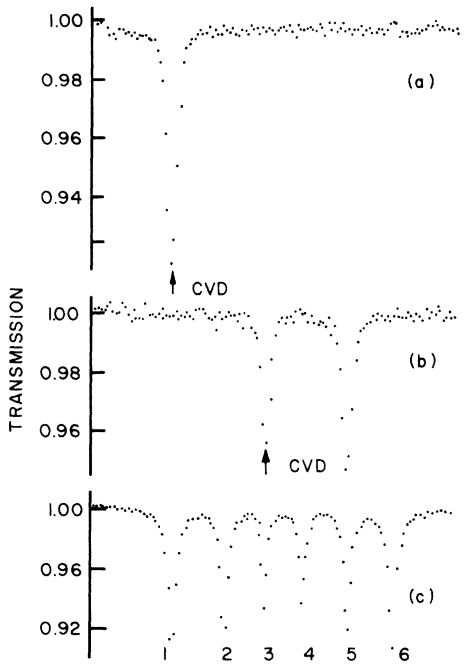

FIG. 5. (a) Experimental SEDM result for a 90%-enriched α-Fe_2O_3 scatterer at room temperature when line 1 is excited. (b) Same as (a) except line 3 is excited. (c) Full transmission spectrum for a 90%-enriched α-Fe_2O_3 absorber at room temperature.

spectrum contains a single line, and the only process is the Mössbauer resonant effect, i.e., $\mu_e = \sigma_R = 0$. In this calculation the CVD is set to excite the sample three natural linewidths off resonance. The results are shown in Fig. 6. There are several observations to be made. First as the thickness of the scatterer increases, i.e., as β increases, the resulting emission line shape is peaked closer and closer to the excitation energy. Notice further that all the peaks are asymmetric. The reason for this is that, due to thickness, the "effective" absorption cross section of the scatterer becomes very broad in energy. However, it is only for very thick scatterers that the effective absorption cross section is constant over the incident-beam energy profile resulting in a completely symmetric line. On the other hand, as β decreases we approach the "single nucleus" limit as calculated classically by Moon[19] and emphasized by Boyle and Hall.[13] In this limit the emission line shape has two peaks, one at the excitation energy and the other at the resonance energy. However, both peaks are *extremely* small compared to the results for thicker scatterers.

Now using the appropriate (A_R/A_M) values the calculated SEDM line shape for a real iron powder is shown in Fig. 7 when the sixth line is excited on resonance and at higher energies. In these calculations we include Rayleigh and incoherent thickness effects. The first point to notice is that in all cases the peak of the SEDM line comes at the energy of the incoming beam as set by the CVD. These calculations were made for two different types of samples: (1) a 90%-enriched iron-powder scatterer and (2) a natural iron-powder scatterer both having a $\beta = 286$. Notice in Fig. 7 a difference between the calculated results is seen for the two different samples only for excitation 10Γ off resonance. Whereas the line shapes for (1) and (2) are very similar, the main contributions to the two lines are different. For case (1), i.e., the enriched iron powder, 95% of the peak is due to Mössbauer scattering and 5% to Rayleigh scattering. For case (2), i.e., the natural iron powder, only 25% is due to Mössbauer scattering, and the rest is due to Rayleigh scattering. Notice also that, as a result, case (1) (see Fig. 6) is slightly less symmetrical than case (2). The difference between the relative contributions of Mössbauer and Rayleigh processes is more clearly exhibited in Fig. 8. In this figure we assume that the fifth line in an iron-powder scatterer is excited. In this case only the peaks on the right contain a Rayleigh contribution. Cases (1) and (2) correspond to the same type of scatterer as assumed for Fig. 7. Now, however, the SEDM spectrum consists of two peaks due to the magnetic dipole selection rule. The ratio of the two peak intensities for the enriched sample changes only slightly in cases (i), (ii), and (iii). However, for the natural sample the change in the ratio is much larger, reflecting the increased relative importance of the Rayleigh contribution. It is clear that an experiment such as this can determine σ_R. We see that Mössbauer processes dominate Rayleigh effects for enriched scatterers excited off resonance by less than 10Γ.

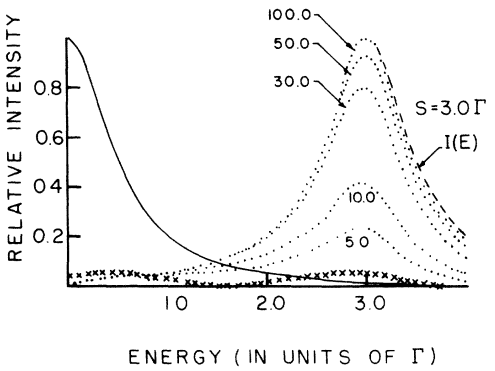

FIG. 6. Calculated emission line shapes for ideal resonant scatterers. The numbers labeling the curves indicate the thickness (β) of the hypothetical scatterers. The setting of the CVD, i.e., the Doppler shift, is 3Γ.

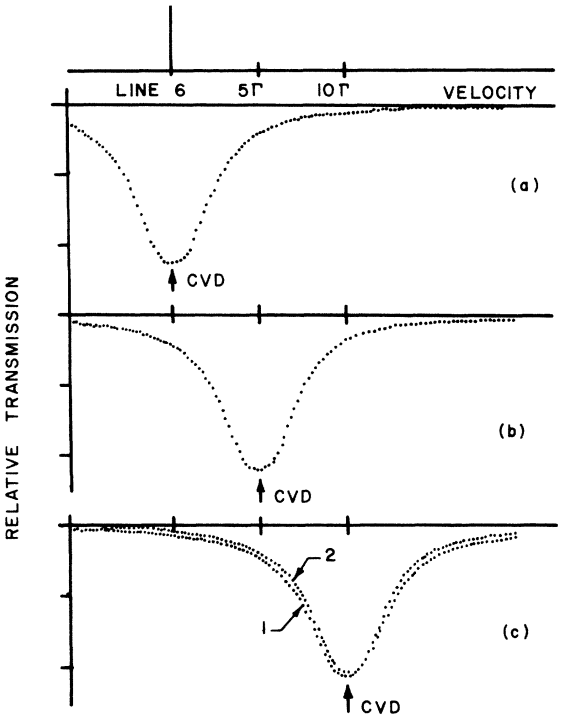

FIG. 7. Calculated SEDM results for an iron-powder scatterer when the sixth line is excited (a) on resonance, (b) 5Γ off resonance, and (c) 10Γ off resonance. In (c) curve 1 is for a 90%-enriched sample and curve 2 is for a natural sample. Notice that cases 1 and 2 give the same results for situations *a* and *b*. The vertical scales are not to be compared for *a*, *b*, and *c*. The normalization was chosen the same so that each figure is clearly presented. In reality the percentage effect decreases as the excitation moves off resonance (see Figs. 9 and 10).

However, for natural scatterers excited 10Γ off resonance, the SEDM peak is almost all due to Rayleigh scattering. This can be clearly seen by looking at the peak on the right-hand side of Fig. 8 for case (2). We have indicated by 2′ the pure Mössbauer contribution to case (2). Notice, that 2′ gives a hint of a peak at the resonance position of line 5, but these effects are completely obliterated by the large Rayleigh contribution. We have experimental results for a natural iron-powder sample excited on resonance, and an enriched iron-powder sample excited off resonance, which substantiate these calculations.

In order to check our calculations further we perform SEDM experiments on a 90%-enriched iron powder at room temperature (298 K) and a 90%-enriched α-Fe_2O_3 powder at liquid-nitrogen temperature (77 K). The CVD was set to excite the sixth line on resonance and two values off resonance for each of these samples. The trapezoidal-function generator in each case was set to sweep the velocity range of the analyzer over a region which contains the sixth peak. In Fig. 9 we show our results for iron powder. Figure 10 gives similar results for enriched α-Fe_2O_3 at liquid-nitrogen temperature. The dots are the experimental results. The solid curve gives the calculated result using the above equations. The calculated results involve two parameters namely, (A_R/A_M) and the over-all percentage effect for *one* spectrum in each figure. The decrease in the percentage effect owing to excitations off resonance follows from our calculations. Notice that the theory correctly predicts the change in the percent effect owing to moving off resonance, the peak position, and the *total* line shape. Observe in Fig. 10 that for excitations off resonance the line shape is slightly asymmetric. This is the result of fact that (A_R/A_M) is small and so the Mössbauer resonant process is dominant (see Fig. 6). The agreement between theory and experiment seems quite satisfactory.

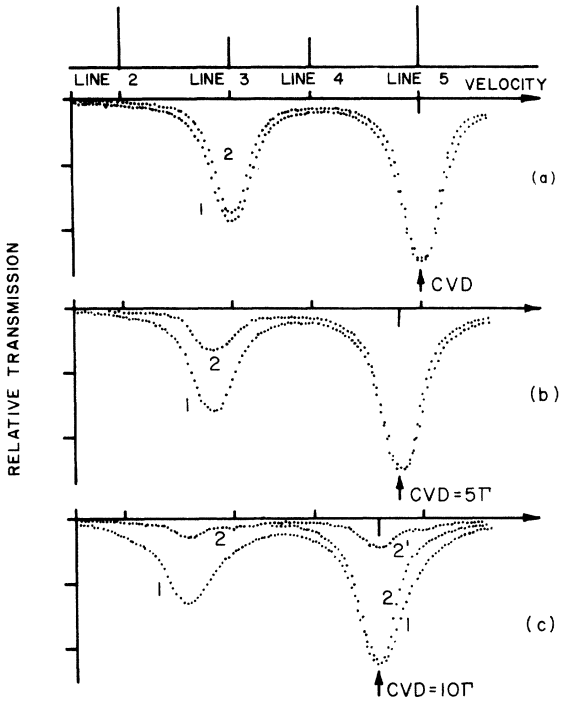

FIG. 8. Calculated SEDM results for an iron-powder scatterer when the fifth line is excited (a) on resonance, (b) 5Γ off resonance, and (c) 10Γ off resonance. The curve labeled 1 correspond to a 90%-enriched sample and curves 2 to a natural sample. Curve 2′ in (c)shows the nuclear resonant contribution to the peak. The vertical scales are not to be compared for *a*, *b*, and *c*. The normalization shown was chosen so that the details of each spectrum could be clearly presented. In reality, the percentage effect decreases as the excitation moves off resonance.

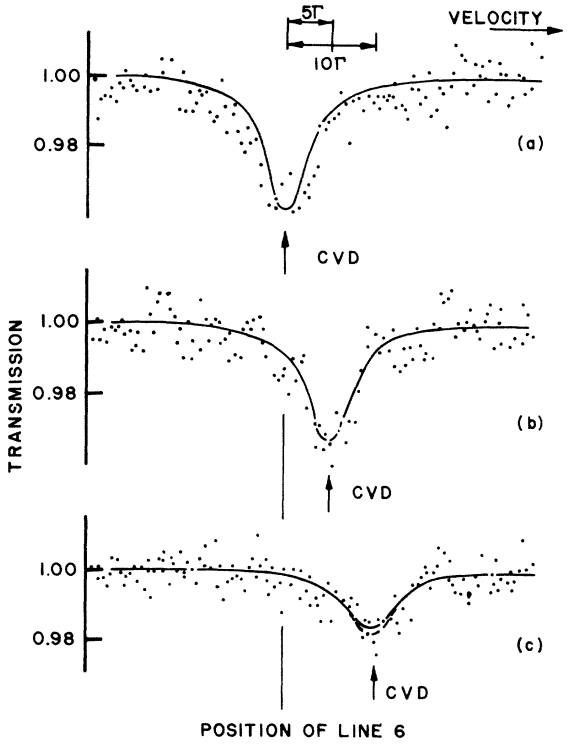

FIG. 9. Experimental SEDM spectra for an enriched iron scatterer at room temperature. In (a) line 6 is excited on resonance, (b) line 6 is excited 5Γ off resonance, and (c) line 6 is excited 10Γ off resonance. The solid curves are the calculations based on Sec. III. The difference between the dashed and solid curves in (c) shows the Rayleigh contribution.

IV. THEORETICAL SEDM RESULTS IN A FLUCTUATING ENVIRONMENT

If the effective fields at the ^{57}Fe nuclei in the scatterer are time dependent, the expected SEDM result is different from that discussed in Sec. III. To obtain the SEDM line shape with relaxation occurring in the scatterer, the effect of the time-dependent fields has to be included in the expression for the scattering line shape given in Eq. 9. This can perhaps be done following Blume's procedure.[20] In such an approach the effective hyperfine fields are written as explicit functions of time by introducing a stochastic model. The central part of the calculation then involves the determination of the correlation function as described by Anderson[21] for the case of transmission geometry. To find the scattering line shape the appropriate stochastic average of Eq. (9), including the time-dependent fields, has to be obtained. In general, the SEDM problem is more difficult than the calculation for the transmission case, and has not yet been solved in general. We will use a less-general approach which is only valid for excitation on resonance. In this second method we made the necessary modifications of the well-known emission line-shape formula needed for the SEDM case. Following Abragam[22] we write for the line shape as a function of energy ω,

$$I(\omega) = \mathrm{Re}[\vec{W} \cdot \underline{A}^{-1} \cdot \vec{I}], \tag{14}$$

where $\vec{W}$ is the probability vector for the ionic states which produce effective fields at the ^{57}Fe nuclei and is time independent for an equilibrium siutation, $\vec{I}$ is a unit vector, $\underline{A} = i(\underline{\omega} - \omega\,\underline{1}) + \underline{\pi}$, where $\underline{1}$ is the unit matrix, $\underline{\pi}$ is the probability matrix for transitions between the ionic states, and $\underline{\omega}$ is the diagonal energy matrix.

Consider the ordinary transmission situation and suppose also a two-level ionic system with both states equally probable. Then Abragam[22] shows that,

$$\pi = \begin{bmatrix} -\Omega & \Omega \\ \Omega & -\Omega \end{bmatrix}, \tag{15}$$

where Ω is the relaxation rate and

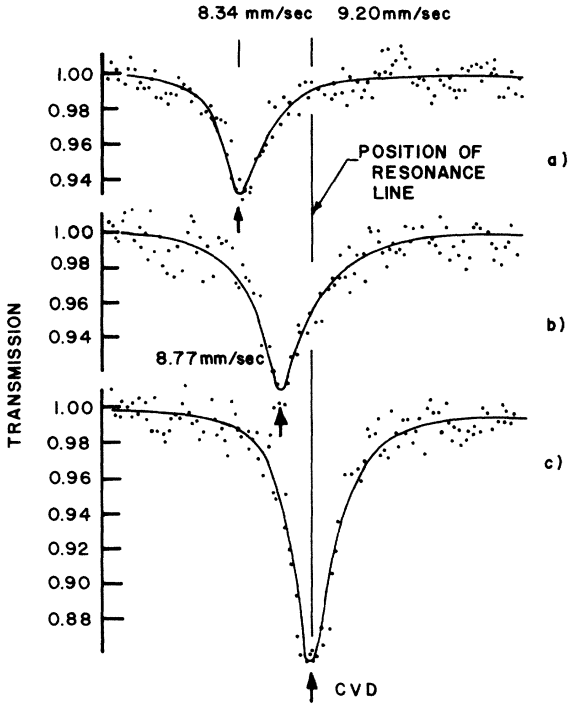

FIG. 10. Experimental SEDM spectra for an enriched α-Fe_2O_3 scatterer at 77 K. In (a) line 6 is excited 8.85Γ off resonance, (b) line 6 is excited 4.43Γ off resonance, and (c) line 6 is excited on resonance. The solid curves are calculations based on Sec. III. The asymmetry in Parts (a) and (b) is due to excitation off resonance (see Sec. III).

$$\underline{A}^{-1} = \frac{1}{\det \underline{A}} \begin{bmatrix} -i(\omega+\delta)-\Omega & -\Omega \\ -\Omega & i(-\omega+\delta)-\Omega \end{bmatrix} , \tag{16}$$

where $\pm\delta$ are the eigenvalues of $\underline{\omega}$, i.e., 2δ equals the nuclear energy difference corresponding to the two possible ionic states.

The line shape for this case can be found by using Eqs. (14)–(16) and noting that $\vec{W} = (\frac{1}{2}, \frac{1}{2})$. The result is,

$$I(\omega) = \frac{-2\Omega\delta^2}{(\delta^2-\omega^2)+4\omega^2\Omega^2} . \tag{17}$$

We now want to calculate a relaxation line-shape expression appropriate for SEDM experiments. Consider an experiment where the CVD is set to excite one of the lines in the scatterer (we are assuming here a situation where even with relaxation they can still be resolved), say the one located at $\omega = +\delta$, corresponding to the ionic spin value $S_z = -\frac{1}{2}$. If there were no relaxation or if $\Omega \sim 0$ we would expect the reemitted radiation to have a peak at $\omega = +\delta$ only.

Suppose we now allow Ω to increase to a value large enough so that there is a reasonable probability for the ionic spin to flip to the other orientation, $S_z = +\frac{1}{2}$. There is now a finite probability for the nucleus to "see" a magnetic field in the opposite direction during the nuclear lifetime and consequently a peak at $\omega = -\delta$ should appear in the SEDM spectrum.

In the analysis of this situation, it is still appropriate to consider the ionic spin-flipping process to be Markovian. It is not stationary, however, since the ionic spin probabilities P_{I} and P_{II} change with time.

If at time $t = 0$, the nucleus is excited and sees a field corresponding to $S_z = +\frac{1}{2}$, what is the probability of its seeing the field due to $S_z = -\frac{1}{2}$ at a later time? We know from Markov-process calculations[23] that,

$$\vec{W}(t) = \begin{bmatrix} P_{\mathrm{I}}(t) \\ P_{\mathrm{II}}(t) \end{bmatrix} = \begin{bmatrix} \frac{1}{2}(1+e^{-2\Omega t}) \\ \frac{1}{2}(1-e^{-2\Omega t}) \end{bmatrix} , \tag{18}$$

when only one state is initially populated but the states are equally likely at equilibrium. Thus P_{II} increases, while P_{I} decreases with time until each equals $\frac{1}{2}$.

To obtain the average probabilities we need to average Eq. (18) over the nuclear lifetime. The result is

$$\bar{W} = \begin{bmatrix} \frac{\Omega+\Gamma}{(2\Omega+\Gamma)} \\ \frac{\Omega}{(2\Omega+\Gamma)} \end{bmatrix} = \begin{bmatrix} W_1 \\ W_2 \end{bmatrix} . \tag{19}$$

For our purposes we must generalize Eq. (19) to include the case when the equilibrium populations of two ionic states are not equal, i.e., $(P_{\mathrm{I}}/P_{\mathrm{II}}) = k$. This gives

$$\bar{W} = \begin{bmatrix} \frac{k\Omega+\Gamma}{\Gamma+(1+k)\Omega} \\ \frac{\Omega}{\Gamma+(1+k)\Omega} \end{bmatrix} . \tag{20}$$

In addition to the above, we need to modify $\underline{A}^{-1}$ [Eq. (16)] to include the natural linewidth Γ as discussed by Abragam.[22]

The result for the selectively excited emission line shape including relaxation between two ionic levels is,

$$I(\omega) = \frac{(a\Delta^+ - \Delta^-)[\Gamma\omega + \Omega(\Delta^+ - a\Delta^-)] - (1+a)\gamma(\Delta^+\Delta^- + \frac{1}{2}\Gamma\gamma)}{(\Delta^+\Delta^- + \frac{1}{2}\Gamma\gamma)^2 + [\Gamma\omega + \Omega(\Delta^+ - a\Delta^-)]^2} , \tag{21}$$

where

$$\Delta^+ = \omega + \delta, \quad \Delta^- = -\omega + \delta, \quad \gamma = (a+1)\Omega + (\tfrac{1}{2}\Gamma),$$

$$a = (\Gamma/\Omega) + k .$$

In Figs. 11 and 12 we show the final SEDM line shapes including analyzer thickness for different values of the various parameters as noted on the figures. In general we note that the difference in two peak heights depends on the ratio of the relaxation rate to nuclear lifetime (Ω/Γ). In addition the lines will be broadened according to the ratio of the relaxation rate to the energy splitting ($\Omega/2\delta$) just as in ordinary transmission results.

The superiority of the SEDM technique over the usual approaches to the study of time-dependent effects can be demonstrated by a direct comparison of the calculated results for the two types of experiments. We consider a hypothetical case where the two peaks are 35 natural linewidths apart and calculate the line shapes for several relaxation rates. Figure 13 shows the calculated transmission spectra and the coresponding results appropriate for the SEDM experiment. Line broadening effects due to the analyzer thickness ($\beta_a = 14$) were included in the calculations. In Fig. 13(a) the curves labeled 1 and 2 are virtually the same

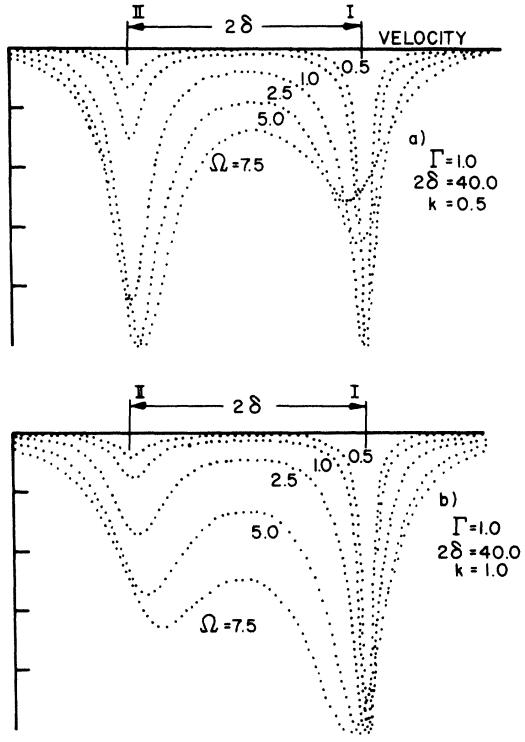

FIG. 11. Calculated SEDM relaxation spectra for different ionic population ratios $k = P_I/P_{II}$. The excitation occurs at line I and $2\delta/\Gamma = 40$. Γ, δ, and Ω are expressed in energy units.

as the result for no relaxation. Curves 3 and 4 show a slight broadening which under experimental conditions may be difficult to identify positively as due to relaxation, since other effects such as sample thickness, collimation, and field inhomogeneities cause a similar modification in the line shape if not accounted for properly. However the SEDM results show the appearance of a second peak in all four cases and thus unambiguously determine the existence of relaxation in the scatterer.

V. APPLICATION OF SEDM TO α-Fe_2O_3

We have used our SEDM techniques to study the Morin transition in α-Fe_2O_3. The rhombohedral crystal hematite (α-Fe_2O_3) is basically antiferromagnetic up to the Néel temperature ($T_N = 946$ K) but also has many other interesting magnetic properties.[24] In particular it has a spin-flip transition at $T_M = 263$ K which is called the Morin transition.[25] Below T_M the antiferromagnetic axis is along the [111] direction while above T_M the spins lie in the (111) basal plane (see Fig. 14). The electric field gradient (EFG) principal axis is along the [111] direction for temperatures both above and below T_M. This transition region has been studied experimentally[25–28] and also theoretically.[29] Ordinary Mössbauer experiments[30] show that above T_M the characteristic six line hyperfine pattern is different from the one observed at low temperatures (see Fig. 15). This is due to the change in relative orientation of the EFG principal axis and the direction and magnitude of the effective internal magnetic field at the ^{57}Fe nuclei.[30] The difference in the Mössbauer spectra can be characterized by noting the positions of the most energetic transition at room (8.34 mm/sec) and liquid-nitrogen (9.20 mm/sec) temperatures relative to a Co-Cu source (see Fig. 15). Regular Mössbauer transmission experiments near T_M show the presence of both hyperfine patterns broadened and partially resolved. Is this because both hyperfine interactions are present and the observed spectrum is simply a superposition of the two, or is each iron ion's spin flipping between the two possibilities? One could extract possible time-dependent information by applying standard relaxation theory to these ordinary Mössbauer spectra.[31] Such an approach is very difficult in this case because the two hyperfine patterns differ only slightly from each other. SEDM experiments obviate this difficulty as discussed above.

In order to apply the relaxation results of Sec.

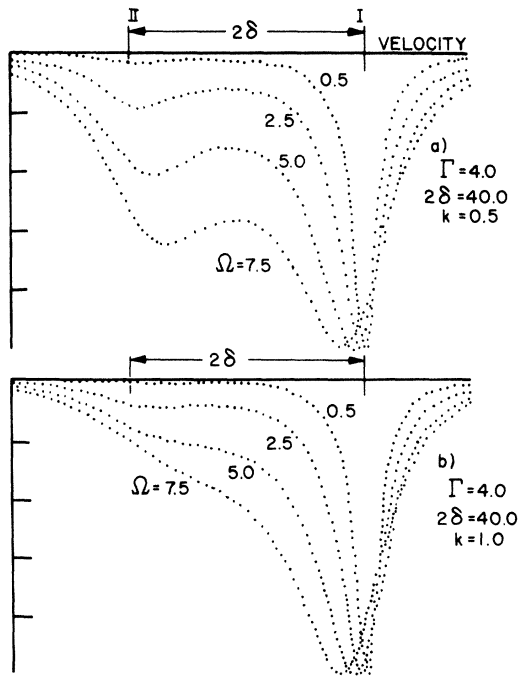

FIG. 12. Calculated SEDM relaxation spectra for different ionic population ratios $k = P_I/P_{II}$. The excitation occurs at line I and $2\delta/\Gamma = 10$. Γ, δ, and Ω are expressed in energy units.

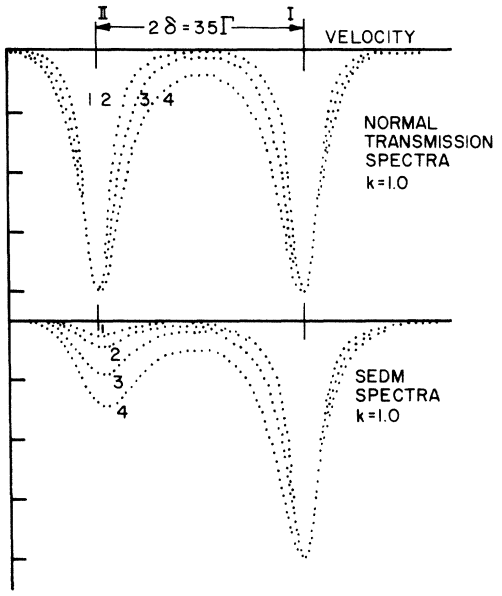

FIG. 13. Calculated relaxation spectra using (a) ordinary Mössbauer transmission geometry, and (b) SEDM assuming relaxation rates in energy units: (1) 0.25Γ, (2) 0.5Γ, (3) 1.25Γ, and (4) 2.5Γ.

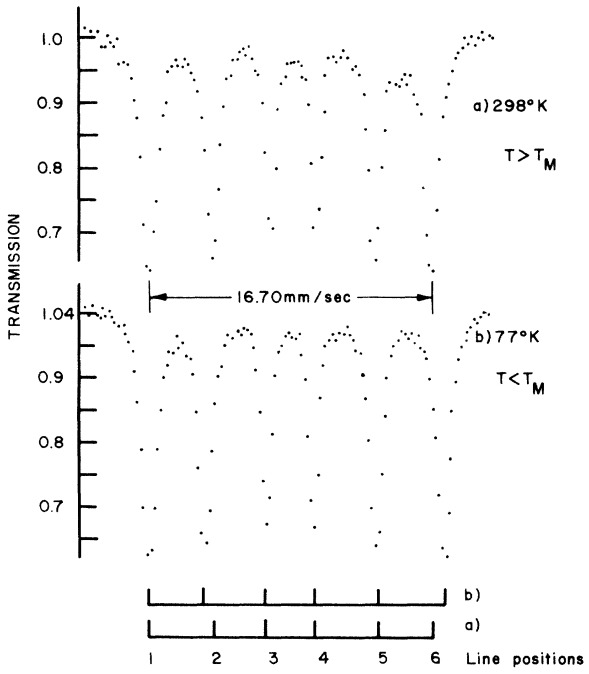

FIG. 15. Transmission spectra of a 90%-enriched sample of α-Fe_2O_3 showing the two different hyperfine patterns (a) above and (b) below T_M.

IV, we needed to know the equilibrium populations of the two ionic states [Eq. (20)]. For this purpose a series of ordinary transmission runs were done using a thin ($\beta = 1$) sample of powdered α-Fe_2O_3. This thin sample was used, in contrast with the thick one of the same material for SEDM, in order to obtain narrower lines and hence better energy resolution. The trapezoidal-function generator was again set to run only over the velocity range of the sixth peak. The results are shown in Fig. 16. From this figure we see that at room temperature one observes a single line which corresponds to the room-temperature hyperfine pattern. At lower temperatures a second line corresponding to a different hyperfine interaction appears and becomes increasingly more intense until at $T_M = 263.5$ K, the two lines are of about equal intensity. Below T_M line II increases at the expense of line I. The bottom spectrum in Fig. 16 was obtained at 77 K and shows a single narrow line at 9.20 mm/sec. A computer program was used to obtain the best two-line Lorentzian fit to the experimental data. From these data the equilibrium populations of the two ionic spin states P_I and P_{II} were obtained as a function of temperature. These values were used in generating the necessary theoretical SEDM relaxation spectra.

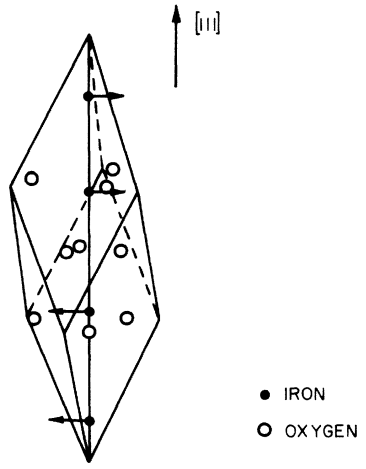

FIG. 14. Unit cell of α-Fe_2O_3. The spin directions indicated correspond to a temperature $T > T_M$.

Our SEDM experiments were performed using a scatterer of 90%-enriched α-Fe_2O_3 powder, i.e., the same material as used for Fig. 16. However, the sample was made thicker to have an effective single-line thickness parameter $\beta = 350$. Our first SEDM experiments were performed with the α-Fe_2O_3 scatterer at 263.5 K. The CVD was set on the energy of the sixth line at room temperature and the analyzer scanned over a velocity range in the neighborhood of the sixth peak. The results are given by the dots in Fig. 17. If these results

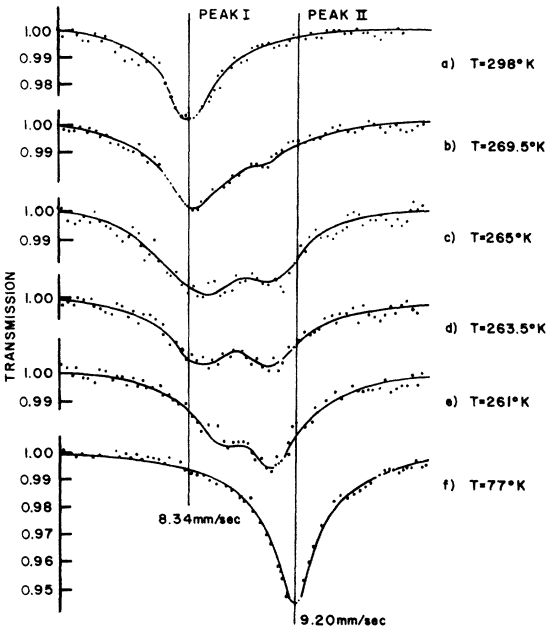

FIG. 16. Transmission spectra in the niighborhood of the most energetic transition in α-Fe_2O_3 at different temperatures in the transition region. The samdle was a thin (β=1) 90%-enriched α-Fe_2O_3 specimen.

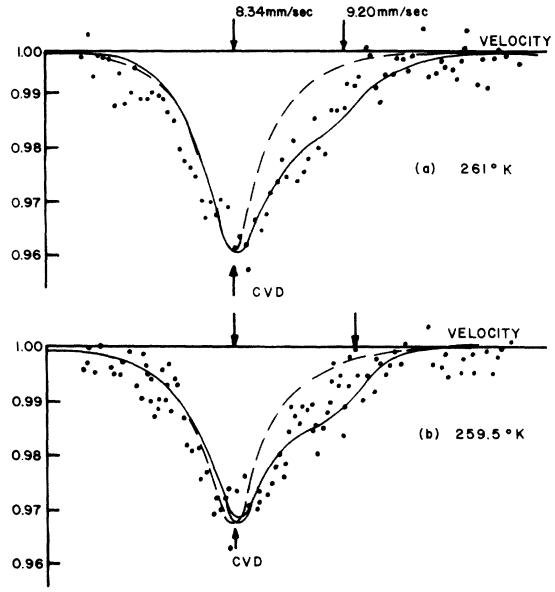

FIG. 18. Experimental SEDM spectra of an enriched α-Fe_2O_3 scatterer at (a) 261 and (b) 259.5 K. The dashed curves are computed according to Sec. III without time-dependent effects. The solid curves are computed results for relaxation times of (a) 2.3×10^7 and (b) 2.9×10^7 sec, respectively.

represent simply a superposition of two static hyperfine patterns, they could be explained by using the results of our time-independent SEDM calculations (Sec. III). One would simply have three contributions: the Rayleigh scattering, the resonant contribution from exciting a peak at or near its resonance (8.34 mm/sec), and another resonant contribution from exciting a second peak *off* resonance. The calculated result according to the time-independent methods of Sec. III is shown in Fig. 17 by the dashed line. The dashed line can also be considered roughly as the sum of experimental spectra obtained by exciting the peak at room temperature near resonance and the peak at liquid-nitrogen temperature off resonance. The liquid-ni-nitrogen peak was actually slightly shifted in our calculations because of the temperature dependence of the internal magnetic field. Notice that the dashed line is quite symmetric. This is to be expected for this case because the major contribution is Mössbauer resonant scattering *on* resonance which is symmetric. The Rayleigh contribution is also symmetric. The asymmetric term arising from resonance scattering *off* resonance is relatively small. However, the solid curve shows the best time-dependent calculated result. Figure 18 shows our results for SEDM experiments done at 259.5 and 261 K. As in Fig. 17 the dots are the data points, the dashed curve gives the theoretical SEDM results *without* relaxation, and the solid curve gives the theoretical SEDM results assuming relaxation. Because of the well-known hysteresis effect, which we also observed, all experiments were done by first going to liquid-nitrogen temperature and approaching each new temperature from the low-temperature side. It is worth emphasizing that the results shown in Figs. 10, 17, and 18 were taken using the *same* sample and geometry *only* the temperature was changed. In comparing Figs.

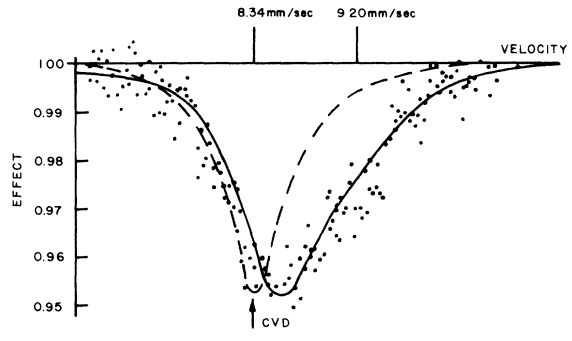

FIG. 17. Experimental SEDM spectrum of an enriched α-Fe_2O_3 scatter at T=263.5 K. The sashed line is computed according to Sec. III without time-dependent effects. The solid curve is the computed result for a relaxation time of 1.1×10^7 sec.

10, 17, and 18 it is important to keep in mind the various contributions to the time-independent SEDM line shape. In addition, notice that the change in the percentage effect with temperature can be made apparent by looking at Fig. 16.

VI. RESULTS AND CONCLUSIONS

We have developed selective-excitation double-Mössbauer (SEDM) calculations that apply to a "split" scatterer, and include Rayleigh, incoherent electronic, and thickness effects. These results can be used to fit experimental SEDM data in the absence of relaxation processes. These calculations show that the exact location and line shape of an SEDM spectrum depend on the physical thickness of the sample, the relative Rayleigh-to-Mössbauer resonant contribution, and the energy difference between the Mössbauer resonant energy and the excitation energy. The consequence of sample thickness for most SEDM cases is to give rise to an "effective" scattering cross section that is very broad compared to the incident beam spread. Thus the result is that the emission line shape appears roughly at the excitation energy but may be asymmetric if the effective scattering cross section is not constant over the incoming beam profile. This will always be true for excitation off resonance but the degree of asymmetry depends on the factors listed above. We have verified these calculations by doing SEDM experimental runs on enriched iron-powder scatterers at room temperature, and on an enriched α-Fe_2O_3 powder scatterer at liquid-nitrogen temperature.

We have further demonstrated the advantage of the SEDM technique in the study of relaxation processes, as compared to the regular Mössbauer transmission procedure (see Fig. 13). We have applied these relaxation procedures to study the Morin transition in α-Fe_2O_3. Our results show that each iron nucleus in α-Fe_2O_3 near the Morin temperature is in a fluctuating hyperfine field. The values of the relaxation times at 263.5, 261, 259.5, and 258.5 K are respectively $(1.1\pm0.2)\times10^{-7}$, $(2.3\pm0.4)\times10^{-7}$, $(2.9\pm0.6)\times10^{-7}$, and $(4.3\pm0.9)\times10^{-7}$ sec.

ACKNOWLEDGMENT

One of us (G. R. H.) would like to thank E. Corinaldesi for a helpful discussion relating to certain aspects of Appendix A.

APPENDIX A

In Sec. III there are various W's which are needed in calculating the result for Eq. (9). We will use the "line" notation as shown in Fig. 4.

$$W_1 = \frac{3}{16\pi}(1+\cos^2\theta),$$

$$W_2 = \frac{1}{4\pi}(1-\cos^2\theta),$$

$$W_3 = \frac{1}{16\pi}(1+\cos^2\theta),$$

$$W_4 = W_3, \quad W_5 = W_2, \quad W_6 = W_1 .$$

To find $\overline{W}$ we need to integrate over all angles. We find,

$$\overline{W}_1 = \frac{1}{4\pi}, \quad \overline{W}_2 = \frac{1}{6\pi}, \quad \overline{W}_3 = \frac{1}{12\pi},$$

$$\overline{W}_4 = \overline{W}_3, \quad \overline{W}_5 = \overline{W}_2, \quad \overline{W}_6 = \overline{W}_1 .$$

We also need the quantities $W_{i,j}(\alpha)$. These are formed by multiplying the angular factor for the absorption process by the angular factor for the emission process and then, since we are dealing with powder samples, integrating over all angles subject to the constraint that the angle between the incoming and outgoing radiation is α. These quantities are

$$W_1 W_1 = W_6 W_6 = \left(\frac{3}{8\pi}\right)^2\left(\frac{1}{4}\right)(1+\cos^2\theta_1)(1+\cos^2\theta_2),$$

$$W_2 W_2 = W_5 W_5 = \left(\frac{3}{8\pi}\right)^2\left(\frac{4}{9}\right)(1-\cos^2\theta_1)(1-\cos^2\theta_2),$$

$$W_3 W_3 = W_4 W_4 = \left(\frac{3}{8\pi}\right)^2\left(\frac{1}{36}\right)(1+\cos^2\theta_1)(1+\cos^2\theta_2),$$

$$W_2 W_4 = \left(\frac{3}{8\pi}\right)^2\left(\frac{1}{9}\right)(1-\cos^2\theta_1)(1+\cos^2\theta_2),$$

$$W_4 W_2 = \left(\frac{3}{8\pi}\right)^2\left(\frac{1}{9}\right)(1+\cos^2\theta_1)(1-\cos^2\theta_2),$$

$$W_3 W_5 = \left(\frac{3}{8\pi}\right)^2\left(\frac{1}{9}\right)(1+\cos^2\theta_1)(1-\cos^2\theta_2),$$

$$W_5 W_3 = \left(\frac{3}{8\pi}\right)^2\left(\frac{1}{9}\right)(1-\cos^2\theta_1)(1+\cos^2\theta_2).$$

The only complication in the averaging process involves an average over $(\cos^2\theta_1\cos^2\theta_2)$ subject to the constraint. This can be done in the following way. Let $\vec{\gamma}_1$ indicate the direction of the incident photon and $\vec{\gamma}_2$ represent the direction of the outgoing photon with respect to a particular $(\vec{i}, \vec{j}, \vec{k})$ coordinate system. Then $\vec{k}\cdot\vec{\gamma}_1 = \cos\theta_1$, $\vec{k}\cdot\vec{\gamma}_2 = \cos\theta_2$, and $\vec{\gamma}_1\cdot\vec{\gamma}_2 = \cos\alpha$. Now if we perform the same rotation R on $\vec{\gamma}_1$ and $\vec{\gamma}_2$, then $R\vec{\gamma}_1\cdot\vec{\gamma}_2 = \cos\alpha$. The necessary average can be found by integrating $(\vec{k}\cdot R\vec{\gamma}_1)^2(\vec{k}\cdot R\vec{\gamma}_2)^2$ over all values of R. This can be done fairly easily by using group theory.[32]

$$\langle\cos^2\theta_1\cos^2\theta_2\rangle = (1/8\pi)\int(\vec{k}\cdot R\vec{\gamma}_1)^2(\vec{k}\cdot R\vec{\gamma}_2)^2 \times(1-\cos\gamma)\,d\gamma\,d\Omega.$$

In this calculation the axis of the rotation R points in the direction subtended by $d\Omega$ and the

angle of rotation about this axis is γ. The above integral allows us to sum over all possible rotations R by summing over all axes and all angles of rotation. It should be noted that $0<\gamma<\pi$. Using the rotation matrix given by Goldstein[33] and performing the above integral gives

$$\langle \cos^2\theta_1 \cos^2\theta_2 \rangle = \frac{1+2\cos^2\alpha}{15}$$

and

$$W_{1,1} = W_{6,6} = \left(\frac{3}{8\pi}\right)^2 \left(\frac{1}{4}\right)\left(\frac{26+2\cos^2\alpha}{15}\right),$$

$$W_{2,2} = W_{5,5} = \left(\frac{3}{8\pi}\right)^2 \left(\frac{4}{9}\right)\left(\frac{6+2\cos^2\alpha}{15}\right),$$

$$W_{3,3} = W_{4,4} = \tfrac{1}{9} W_{1,1},$$

$$W_{2,4} = W_{4,2} = W_{3,5} = W_{5,3} = \left(\frac{3}{8\pi}\right)^2 \left(\frac{1}{9}\right)\left(\frac{14-2\cos^2\alpha}{15}\right).$$

---

†Supported by the National Science Foundation Grant No. GH-39137.

*Portions taken from a dissertation by B. B. submitted in partial fulfillment of the Ph. D. degree.

[1]A. N. Artemev, G. V. Smirov, and E. P. Stepanov, Zh. Eksp. Teor. Fiz. 54, 1028 (1968) [Sov. Phys.—JETP 27, 547 (1968)].

[2]W. Meisel, Monatsber, Dtsch. Akad. Wiss. Berlin Ger. 11, 355 (1969).

[3]N. D. Heiman, J. C. Walker, and L. Pfeiffer, Phys. Rev. 184, 281 (1969).

[4]J. J. Spijkerman and J. R. DeVoe, Natl. Bur. Std. Technical Note No. 276 (U.S. GPO, Washington, D.C., 1966).

[5]F. C. Ruegg, J. J. Spijkerman, and J. J. DeVoe, Rev. Sci. Instrum. 36, 356 (1965).

[6]R. L. Cohen, Rev. Sci. Instrum. 37, 260 (1966).

[7]W. Gaitanis, A. Kostikas, A. Simopoulos, Nuclear Research Center Democritos, Athens, Greece (unpublished).

[8]L. T. Swartzendruber, Nucl. Instrum. Methods 69, 101 (1969).

[9]M. Alam, Ph. D. dissertation (Boston University, 1966) (unpublished).

[10]Yu. Kagan, A. M. Afansév, and I. P. Perstnev, Zh. Eksp. Teor. Fiz. 54, 1530 (1968) [Sov. Phys.—JETP 27, 819 (1968)].

[11]See, for example, G. R. Hoy and S. Chandra, J. Chem. Phys. 47, 961 (1967).

[12]W. Heitler, *Quantum Theory of Radiation* (Clarendon, Oxford, 1954), pp. 196–204.

[13]A. J. F. Boyle and H. E. Hall, Rep. Prog. Phys. 25, 441 (1962), pp. 455–459.

[14]P. Debrunner and R. J. Morrison, Rev. Sci. Instrum. 36, 145 (1965).

[15]P. B. Moon, Proc. Phys. Soc. Lond. A63, 80 (1950).

[16]P. J. Black, G. Longworth, and D. A. O'Connor, Proc. Phys. Soc. Lond. 83, 937 (1964).

[17]P. J. Black, D. E. Evans, and D. A. O'Connor, Proc. R. Soc. Lond. A270, 168 (1962).

[18]W. Renz and H. Appel, in *Hyperfine Structure and Nuclear Radiations*, edited by E. Matthias and D. A. Shirley (North-Holland, Amsterdam, 1968), p. 370.

[19]P. B. Moon, Proc. R. Soc. Lond. A263, 309 (1961).

[20]M. Blume, in *Hyperfine Structure and Nuclear Radiations*, edited by E. Matthias and D. A. Shirley (North-Holland, Amsterdam, 1968), p. 911.

[21]P. W. Anderson, J. Phys. Soc. Jap. 9, 316 (1954).

[22]A. Abragam, *Nuclear Magnetic Resonance* (Oxford U.P., London, 1961).

[23]A. Paupolis, *Probability, Random Variables, and Stochastic Processes* (McGraw-Hill, New York, 1965).

[24]P. J. Flanders and J. P. Remeika, Philos. Mag. 11, 1271 (1965).

[25]P. Imbert and A. Gerard, C. R. Acad. Sci. (Paris) 257, 1054 (1963).

[26]S. T. Lin, Phys. Rev. 116, 1447 (1959).

[27]R. C. Liebermann and S. K. Banerjee, J. Appl. Phys. 41, 1414 (1970).

[28]S. Foner and S. J. Williamson, J. Appl. Phys. 36, 1154 (1965).

[29]J. O. Artman, J. C. Murphy, and S. Foner, Phys. Rev. 138, A912 (1965).

[30]F. Van der Woude, Phys. Status Solidi 17, 417 (1966).

[31]H. H. Wickmann, *Mössbauer Effect Methodology*, edited by I. J. Gruverman (Plenum, New York, 1968), Vol. 2, p. 316.

[32]M. Hamermesh, *Group Theory* (Addison-Wesley, Reading, Mass., 1964).

[33]H. Goldstein, *Classical Mechanics* (Addison-Wesley, Cambridge, Mass. 1953), p. 109.